nature research

https://doi.org/10.1038/s41563-020-00871-7

Supplementary information

Evidence for a higher-order topological insulator in a three-dimensional material built from van der Waals stacking of bismuth-halide chains

In the format provided by the authors and unedited

Supplementary Information: Evidence for a higher order topological insulator in a three-dimensional material built from van der Waals stacking of bismuth-halide chains

Ryo Noguchi,[1] Masaru Kobayashi,[2] Zhanzhi Jiang,[3] Kenta Kuroda,[1] Takanari Takahashi,[2] Zifan Xu,[3] Daehun Lee,[3] Motoaki Hirayama,[4] Masayuki Ochi,[5] Tetsuroh Shirasawa,[6] Peng Zhang,[1] Chun Lin,[1] Cédric Bareille,[1] Shunsuke Sakuragi,[1] Hiroaki Tanaka,[1] So Kunisada,[1] Kifu Kurokawa,[1] Koichiro Yaji,[1] Ayumi Harasawa,[1] Viktor Kandyba,[7] Alessio Giampietri,[7] Alexei Barinov,[7] Timur K. Kim,[8] Cephise Cacho,[8] Makoto Hashimoto,[9] Donghui Lu,[9] Shik Shin,[1,10] Ryotaro Arita,[4,11] Keji Lai,[3] Takao Sasagawa*,[2] and Takeshi Kondo*[1,12]

[1]*Institute for Solid State Physics, The University of Tokyo, Kashiwa, Chiba 277-8581, Japan*

[2]*Materials and Structures Laboratory, Tokyo Institute of Technology, Yokohama, Kanagawa 226-8503, Japan*

[3]*Department of Physics, The University of Texas at Austin, Austin, Texas 78712, United States*

[4]*RIKEN Center for Emergent Matter Science (CEMS), Wako, Saitama 351-0198, Japan*

[5]*Department of Physics, Osaka University, Toyonaka, Osaka 560-0043, Japan*

[6]*National Metrology Institute of Japan, National Institute of Advanced Industrial Science and Technology, Tsukuba, Ibaraki 305-8565, Japan*

[7]*Elettra - Sincrotrone Trieste, S.S.14, 163.5 km, Basovizza, Trieste, Italy*

[8]*Diamond Light Source, Harwell Campus, Didcot, OX11 0DE, United Kingdom*

[9]*Stanford Synchrotron Radiation Light source, SLAC National Accelerator Laboratory, 2575 Sand Hill Road, Menlo Park, California 94025, USA*

[10]*Office of University Professor, The University of Tokyo, Kashiwa, Chiba 277-8581, Japan*

[11]*Department of Applied Physics and Quantum-Phase Electronics Center (QPEC), The University of Tokyo, Tokyo 113-8656, Japan*

[12] *Trans-scale Quantum Science Institute,*
The University of Tokyo, Bunkyo, Tokyo 113-0033, Japan
(Dated: December 16, 2020)

SUPPLEMENTARY NOTE 1: PARITY EIGENVALUES OF THE BLOCH FUNCTIONS IN BI_4X_4 (X=I OR BR) [FIG. S1]

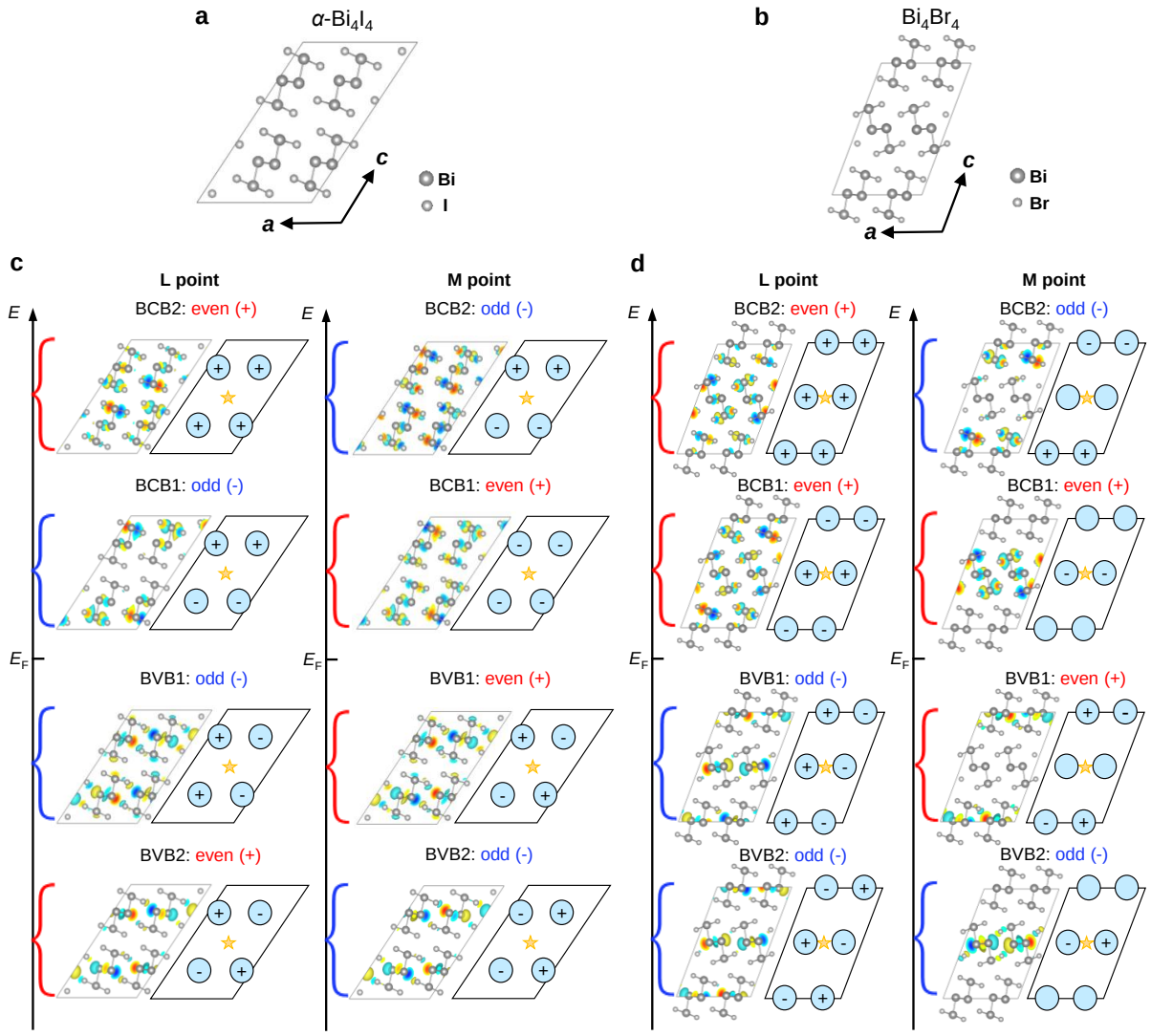

FIG. S1. **a, b,** The unit cell of α-Bi_4I_4 and Bi_4Br_4 used for the visualization of the Bloch functions, respectively. **c, d,** The Bloch functions of two bulk conduction bands (BCB1 and BCB2) and two bulk valence bands (BVB1 and BVB2) close to E_F at the L point and the M point of α-Bi_4I_4 and Bi_4Br_4, respectively. The red (blue) color shows positive (negative) values of the Bloch functions calculated without SOC. The schematics of the Bloch functions are shown on the right of the numerically plotted figures to easily understand the parity eigenvalues, which are shown as even (+) or odd (-). The + and - in the blue circles indicate the phases of the Bloch functions for each quasi-1D Bi_4X_4 chain.

In order to investigate the origin of the different band topology between α-Bi_4I_4 and Bi_4Br_4, we visualized the Bloch function at the L point and the M point of the two compounds. We used the *ab initio* code OpenMX [1] with the PBE functional in the GGA without the spin-orbit coupling (SOC) [2]. We took a 6×6×2 -mesh for Bi_4Br_4 and α-Bi_4I_4. We employed the valence orbital sets Bi8.0-s3p3d3f2, Br7.0-s3p2d1, and I7.0-s3p3d2f1. The energy cutoff for the numerical integration was set to 150 Ry.

As shown in Fig. S1, the order of parity eigenvalues before the inclusion of SOC is $(--;++)$ at the L point only for Bi_4Br_4; this occurs because the position of the inversion center comes to inside of the plane for the AB-stacking, differing from the AA'-stacking of α-Bi_4I_4, where the inversion center is located between the planes. This situation in Bi_4Br_4 leads to the nontrivial second-order topology with $Z_4 = 2$ when the double band inversion takes place under the inclusion of SOC. In contrast, the orders of parity eigenvalues in α-Bi_4I_4 without SOC are $(-+;+-)$ at the M point and $(+-;-+)$ at the L point. Therefore, the band inversions in α-Bi_4I_4 induced by SOC cannot lead to the HOTI state with $Z_4 = 2$.

SUPPLEMENTARY NOTE 2: STRUCTURAL STACKING-DEPENDENCE OF THE PARITY EIGENVALUES EXPRESSED WITH THE BLOCH FUNCTIONS [FIG. S2]

We found that different bulk topologies between α-Bi_4I_4 (trivial insulator) with AA'-stacking and Bi_4Br_4 (HOTI) with AB-stacking originate from a slight shift of the inversion center from one to the other in the unit cell (see Fig. S2). The Bloch functions for Bi_4X_4 (X=I or Br) can be commonly illustrated at the L point, as in Fig. S2. The valence and conduction bands are both split into antibonding and bonding states. In the AA'-stacking (α-Bi_4I_4 case), the inversion center (yellow stars in Fig. S2) is located between the chain-layers, leading to the parity eigenvalues of $(+-;-+)$. The inversion center is shifted to the inside of a plane for the case of AB-stacking (α-Bi_4I_4 case). Interestingly, this causes a variation of the parity eigenvalues to $(--;++)$, which is critical to generate the HOTI phase by the band inversion with SOC.

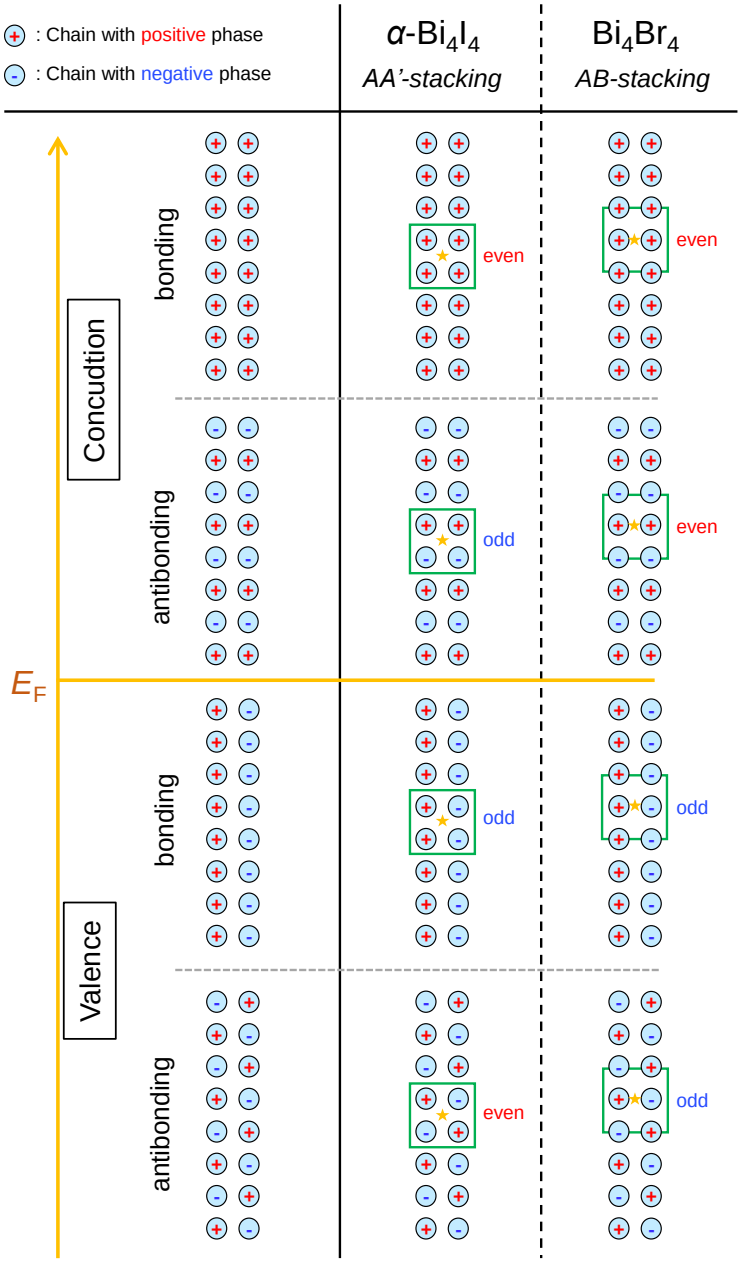

FIG. S2. Schematic of the relation between the unit cells of α-Bi_4I_4 and Bi_4Br_4 and the parity eigenvalues of the Bloch functions without SOC.

SUPPLEMENTARY NOTE 3: CHARACTERIZATION OF BI_4BR_4 CRYSTALS [FIG. S3]

By X-ray diffraction shown in Fig. S3, the crystal structure of Bi_4Br_4 was confirmed to be built from the stacking of Bi_4Br_4 layers rotated alternately by 180 degrees (i.e., the AB-

stacking phase). Particularly we note that no signature of either the hypothetical α-phase (the AA'-stacking phase) or the hypothetical β-phase (the A-stacking phase) of Bi_4Br_4 was detected by the diffraction patterns from the ab-planes of single crystals and from powders (pulverized crystals); notably, the β-phase was theoretically predicted to be a weak topological insulator [3]. Furthermore, any other crystal phases will not be expected either. Only the AB-stacking phase is possible in Bi_4Br_4, thus we do not use a particular phase notation for this compound in our paper.

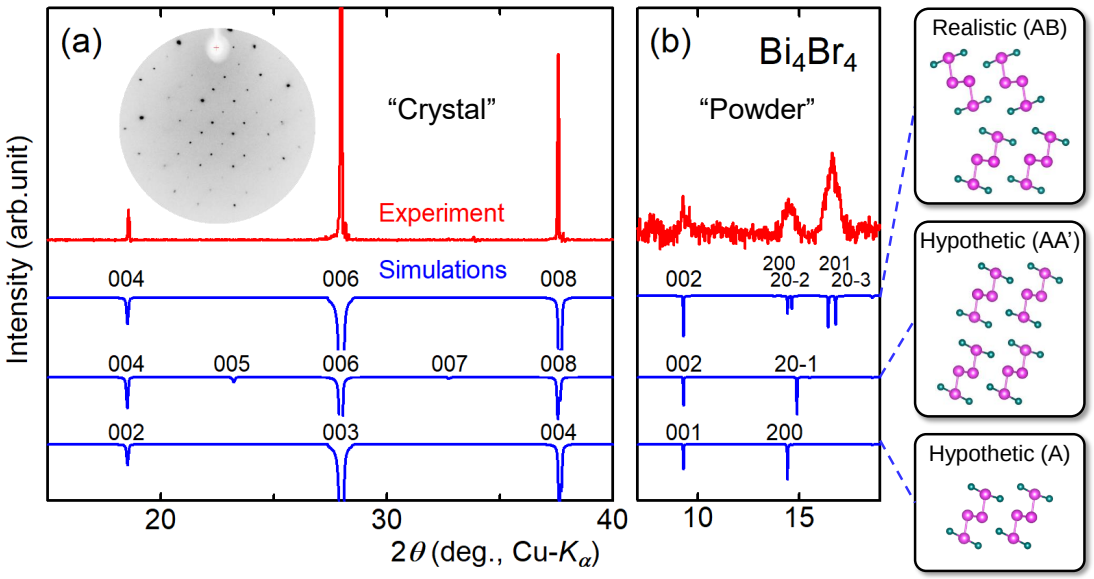

FIG. S3. Experimental (red) and theoretical (blue) X-ray diffraction patterns of Bi_4Br_4 (a) from the ab-planes of single crystals and (b) from the powders (pulverized crystals), respectively. The crystal structure used for the simulations was shown in the right panel. Inset of (a) shows a 2D diffraction pattern obtained from single-crystal X-ray diffraction experiments: by the structural analysis of a set of the diffraction data, the lattice parameters of $a = 13.090$ Å, $b = 4.340$ Å, $c = 20.110$ Å, and $\beta = 107.13°$ were obtained.

SUPPLEMENTARY NOTE 4: CLEAVABLE PLANES OF BI_4BR_4 [FIG. S4]

The Bi_4Br_4 crystal is cleavable both in the top and side planes due to the quasi-1D crystal structure, similarly to β-Bi_4I_4 [4]. Such a feature is observed in the laser-microscope image of a cleaved surface, exhibiting many terraces and facets with small heights (the main Fig. 2d). We have confirmed that these structures indeed come from the top-plane (001) and the side-plane (100) of the crystal by the experiments of grazing-incidence small-angle X-ray

scattering (GISAXS), which clearly show two reflection signals corresponding to these two planes (the main Fig. 2e). In the same GISAXS image, some other structures have also been visible. These should be, however, experimental artifacts such as the scattered light from the slits since the same signatures were constantly observed after rotating the sample by 13°, as demonstrated in Fig. S4. Our results, thus, indicate that the Bi_4Br_4 crystal has only two naturally cleavable planes: the top-plane (001) and the side-plane (100).

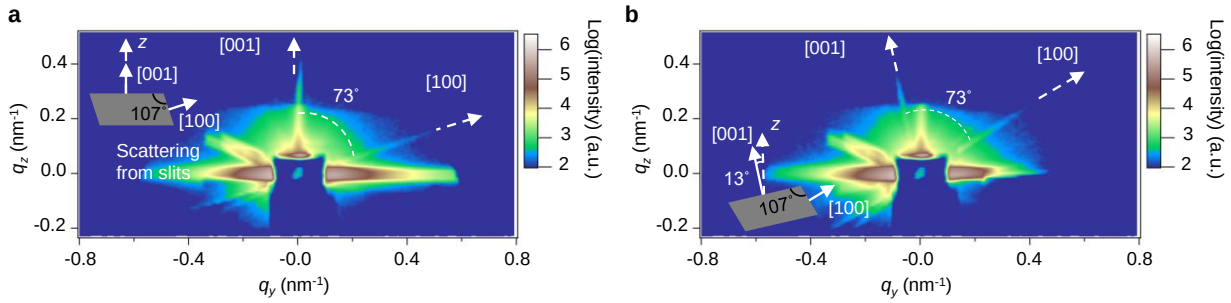

FIG. S4. **a, b,** Grazing-incidence small-angle X-ray scattering (GISAXS) measurement of a cleaved Bi_4Br_4 crystal with different orientation (panel **a** is a duplicate of Fig. 2e). The chain direction of the sample (b axis) was aligned parallel with the incident X-ray in each measurement. The reflection signals from the sample is rotated by around 13° between **a** and **b** due to the different orientation of the sample, while the signals from the experimental apparatus are constantly observed in the same direction. Two strong reflection peaks from the sample are separated by around 73°, consistent with the angle between the (001) and the (100) planes of Bi_4Br_4.

SUPPLEMENTARY NOTE 5: SIMILARITY OF CLEAVAGE SURFACE BETWEEN BI_4I_4 AND BI_4BR_4 [FIG. S5]

In order to verify our conclusion that Bi_4Br_4 is a HOTI, it would be significant to investigate series materials of bismuth halides which can realize different topologies, and explore a HOTI through comparison among them. To assure the reliability of comparing ARPES data, here, we demonstrate that the surface condition we measured by ARPES was very similar between Bi_4Br_4 and Bi_4I_4. The ARPES data were taken from clean surfaces prepared by cleaving single crystals: we attached a piece of tape on the (001) plane and peeled it off in the vacuum chamber. The laser-microscope displays the details of the cleavage surface, revealing complex structures consisting of various steps; this is more clearly demonstrated in Fig. S5, which plots a spectrum of step height along a one-dimensional cut. Significantly,

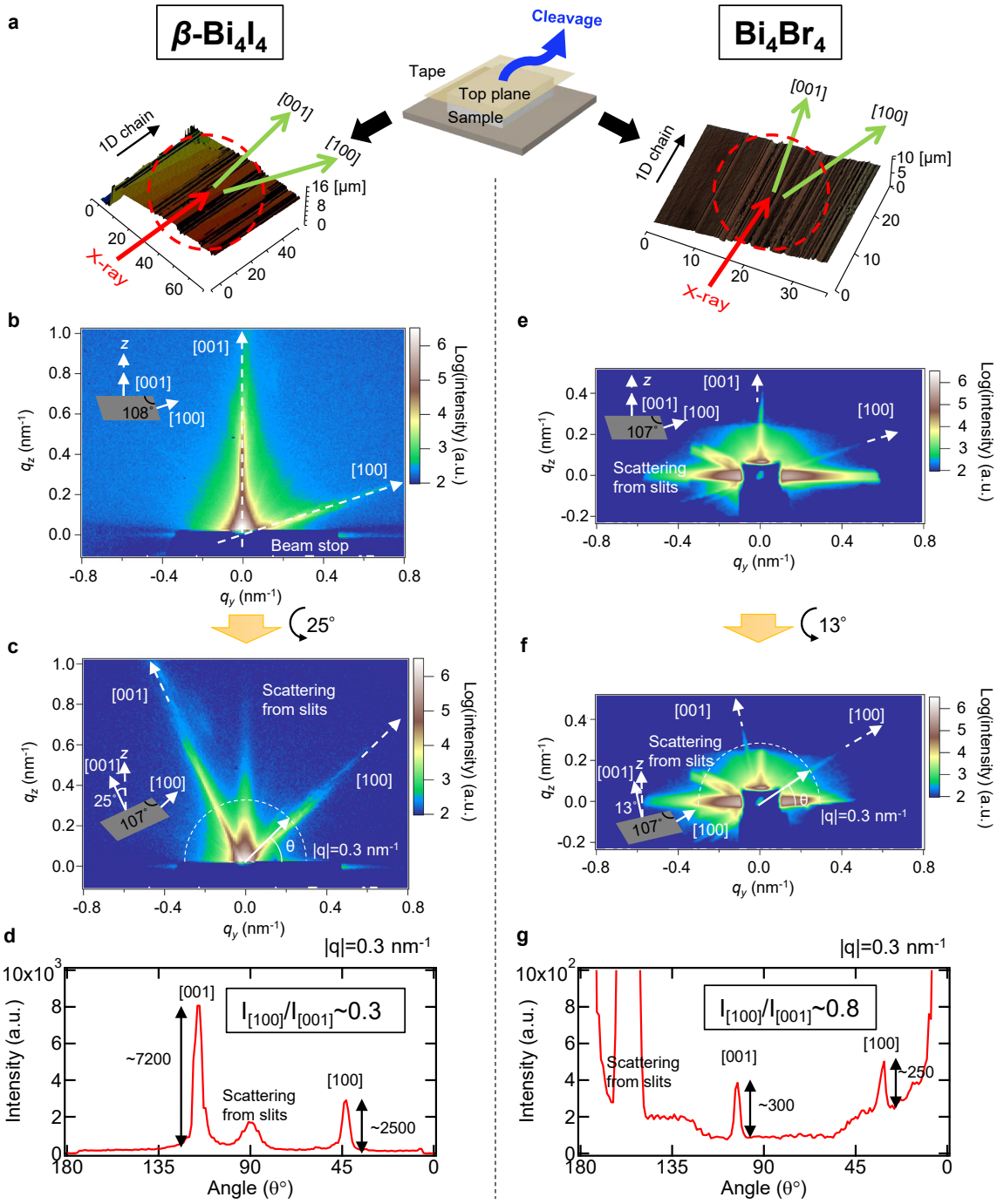

FIG. S5. **a,** Laser microscope images for the cleavage surfaces of β-Bi_4I_4 and Bi_4Br_4, which were obtained by peeling off a piece of tape attached on the *ab*-plane of the crystals; on each image, a schematic of X-ray scattering (or GISAXS) experiment is illustrated by arrows and a dashed curve with about a size of X-ray beam. **b, c,** GISAXS results for β-Bi_4I_4 taken with setting the top (001) plane to be parallel to the q_y axis (**b**) and taken after rotating the sample by 25° to avoid overlapping with the intensities coming from an apparatus slit (**c**). **d,** Angular distribution of GISAXS intensity extracted from **c** at $|q| = 0.3$ nm^{-1}. **e-g,** Same as **b-d**, but for Bi_4Br_4. In **f**, the sample was rotated by 13°. The results for β-Bi_4I_4 have been reproduced from [4].

we found that such a very rough surface consists of only two kinds of planes, the top (001) surface and the side (100) surface, owing to the unique property of Bi_4Br_4 and Bi_4I_4 crystals built from chains connected by the van-der-Waals force (see X-ray scattering data in Figs. S5b and S5e).

To avoid the overlapping of scattering signals from apparatus slits onto the real data, we have rotated the samples by certain angles and taken the scattering image again, as plotted in Figs. S5c and S5f for Bi_4I_4 and Bi_4Br_4, respectively. From these data, the intensity spectra at $|q|$=0.3nm^{-1} are extracted in Figs. S5d and S5g. We find that, while the scattering intensity for the side (100) plane is weaker than that for the top (001) plane, this difference is relatively small: the intensity ratio of $I[100]/I[001]$ is about 0.3 and 0.8 for Bi_4I_4 and Bi_4Br_4, respectively. This indicates that a huge number of side surfaces and hence also of hinge structures are exposed on the cleaved surface we measured by ARPES. More importantly for the current arguments, the results of X-ray scattering revealed that the condition of cleavage surface is similar between Bi_4I_4 and Bi_4Br_4, which thus assures that the ARPES data of these compounds can be fairly compared with each other (see Supplementary Note 11 and Note 12).

SUPPLEMENTARY NOTE 6: LOCAL CONDUCTIVITY IMAGING BY MICROWAVE IMPEDANCE MICROSCOPY [FIG. S6]

In order to obtain spatially resolved information of the topological hinge states, we have performed local conductivity imaging on Bi_4Br_4 by microwave impedance microscopy (MIM) [5]. In this experiment, the 1 GHz microwave is sent to the shielded cantilever probe, and the reflected signal is detected by the MIM electronics. Note that the measured tip-sample impedance maps contain both topographic cross-talk and local electrical information. Quantitative analysis on samples with substantial height variation is therefore challenging. Since the typical step height in cleaved Bi_4Br_4 crystals is too large for scanning probe experiments, we have exfoliated Bi_4Br_4 flakes thinner than $\sim$100 nm on SiO_2/Si substrates (Fig. S6a). Fig. S6b shows the room-temperature atomic-force microscopy (AFM) and MIM images for a ribbon-like flake with a thickness of $\sim$50 nm. On one side (lower edge in this case) of the sample, the MIM signal first increases as the tip approaches the flake and decreases when the tip climbs up the step, which is a clear indication of a topographic

artifact. On the other side (upper edge), however, the MIM map only displays strong peaks at the edges, as seen in Fig. S6b. These features are also confirmed in Fig. S6c, plotting line profiles extracted along red and blue dotted lines in the AFM and MIM images of Fig. S6b, respectively. The same line profiles in Fig. S6c are obtained in both forward and reverse raster scans, i.e., the effect due to tip twisting is minimal. This behavior, as evidenced in Figs. S6d-f, is observed in all (> 10) flakes measured by several (> 5) MIM probes. As a result, the phenomenon cannot be ascribed to simple cross-talk due to the step height and can be potentially taken as signatures of the topological hinge states in Bi_4Br_4.

At this stage, however, we cannot unambiguously establish the presence of topological hinge states by the MIM data. Since the cross-section of Bi_4Br_4 nano-flakes is a slanted parallelogram rather than a rectangle, it is still possible that the tip-sample contact force is systematically different between the two sides, leading to the different MIM signals. A more convincing experiment would be to monitor the evolution of edge signals as a function of

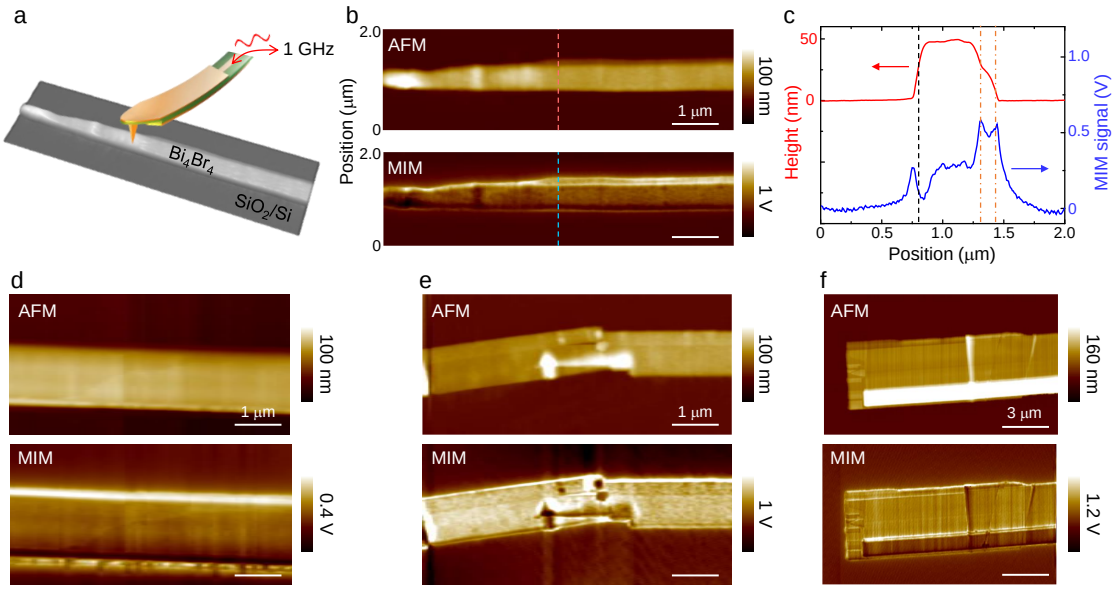

FIG. S6. **a,** Schematics of the MIM setup and Bi_4Br_4 sample on SiO_2/Si. **b,** AFM (top) and MIM (bottom) images of an exfoliated Bi_4Br_4 thin flake. **c,** Line profiles across the Bi_4Br_4 flake, as indicated in the surface topography and MIM images in **b**. The two orange dash-dotted lines mark the edges with high MIM signals. The black dashed line marks the edge with ambipolar MIM signals due to topographic artifact. **d-f,** AFM/MIM images of three more Bi_4Br_4 thin flake samples, showing similar behaviors as **b**. Scale bars are 1 μm in **b, d, e** and 3 μm in **f**.

temperature or magnetic field. Unfortunately, the Bi_4Br_4 flakes are rather fragile and easily broken by the low-temperature contact-mode MIM in our laboratory. Future experiments with good feedback height control in cryogenic setups are necessary to explore the topological hinge states in a spatially resolved manner.

SUPPLEMENTARY NOTE 7: DIMENSION OF TERRACES AND STEPS EXPOSED ON THE CLEAVAGE SURFACE OF BI_4BR_4 [FIG. S7]

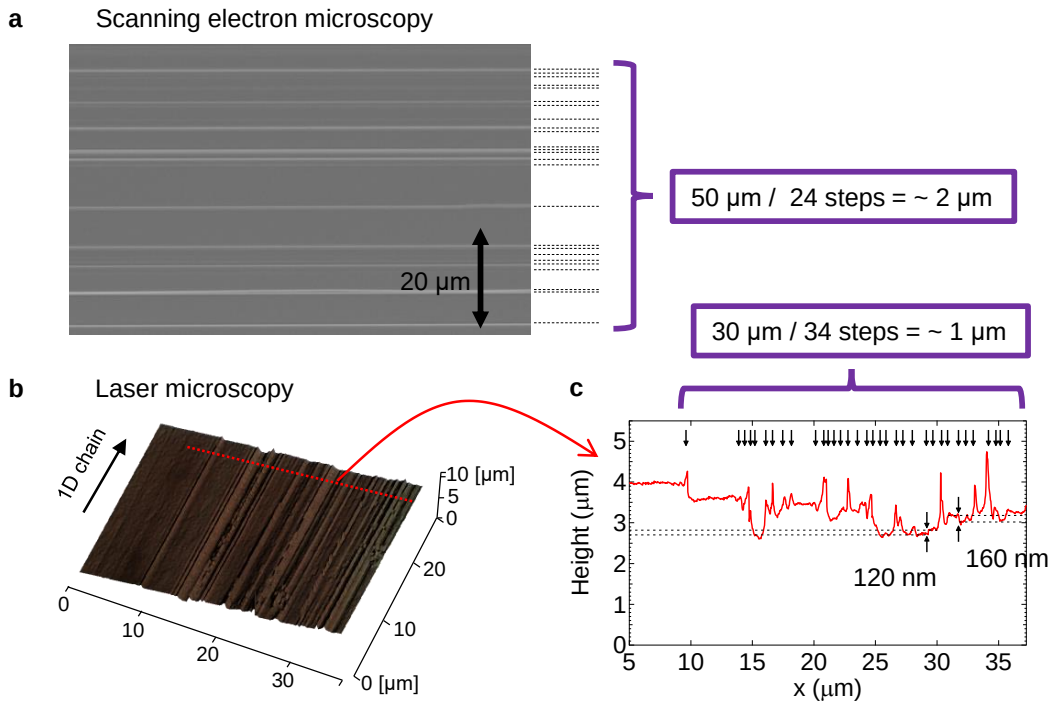

FIG. S7. **a,** SEM image of a cleaved surface in Bi_4Br_4. The black dotted lines mark the step edges running along the b-axis. The average interval between observable steps is estimated to be ~ 2 μm. **b,** Laser-microscope image of a cleaved surface and (**c**) the line profile extracted along the red dotted line in **b**. The average interval between observable steps and the typical height are ~ 1 μm and ~ 100 nm, respectively. The panels of **a** and **b** are duplicates of Figs. 2c and 2d, respectively.

A spectrum of laser-microscope extracted along a one-dimensional cut reveals very complex structures consisting of various steps (Supplementary Fig. S7c). The average distance and typical step hight are estimated to be $\sim$ 1-2 μm and ~ 100 nm, respectively (Supplementary Fig. S7). While actual values for them could be smaller taking account of the spatial

resolutions of SEM and laser-microscopy (∼50-100 Å), these should still be much larger than the confinement dimension (∼10Å: the thickness of a single chain) of the topological hinge states theoretically predicted [6], and thus the hinge states would be well separated without interfering from each other in the real space.

SUPPLEMENTARY NOTE 8: FIRST-PRINCIPLES CALCULATION OF THE BULK BAND STRUCTURES IN BI_4BR_4 [FIG. S8]

Here we show DFT calculations of Bi_4Br_4 along the momentum cuts where the ARPES data in the main Fig. 3 and Fig. 4 were measured; the calculation method is explained in the method section. Fig. S8a shows the bulk band dispersions along the $\bar{M}$-$\bar{\Gamma}$-$\bar{M}$ line, which corresponds to the intensity map of synchrotron-based ARPES plotted in the main Fig. 3g. In Figs. S8b and S8c, we also exhibit the DFT dispersions along the chain direction across $\bar{\Gamma}$ and $\bar{M}$, corresponding to the ARPES images in the main Figs. 3h and 3i, respectively. A relatively good agreement is obtained between DFT and ARPES dispersions.

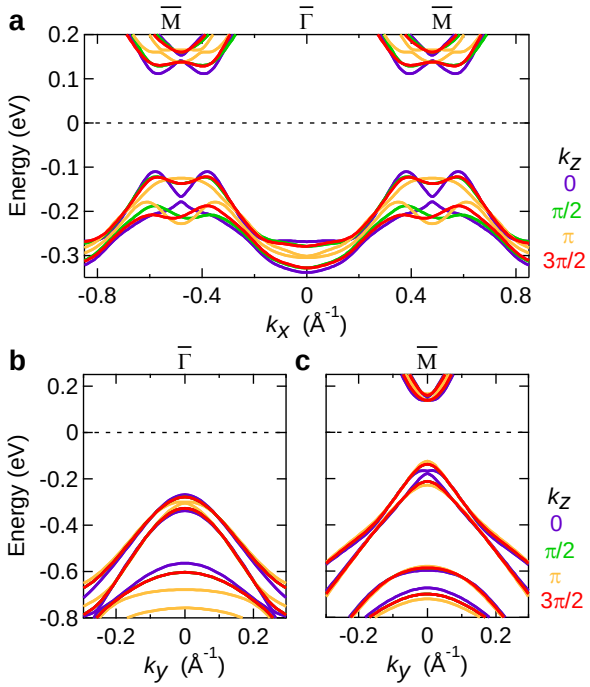

FIG. S8. **a,** Projected bulk bands for the top-surface (001) along the $\bar{M}$-$\bar{\Gamma}$-$\bar{M}$ line. **b, c,** Projected bulk bands for the top-surface (001) around the $\bar{\Gamma}$ point (**b**) and the $\bar{M}$ point (**c**) cut along the chain direction of the crystal (k_y direction). The colors of the lines denote different k_z values.

SUPPLEMENTARY NOTE 9: ELECTRONIC STRUCTURE FOR THE SIDE-SURFACE (100) SELECTIVELY MEASURED BY NANO-ARPES [FIG. S9]

We performed nano-ARPES to selectively observe the band structure of the side-surface (100) at the Spectromicroscopy beamline of Elettra light source [7]. A Schwarzschild objective was used to focus the photon beam to a spot of less than 1 μm in size, enabling the observation of the photoelectrons emitted from the side-surface (100). The obtained photoemission distributions do not show any observable dispersions along k_z within the experimental resolution of $\Delta E \sim 60$meV (Figs. S9c and S9d), in sharp contrast to the data

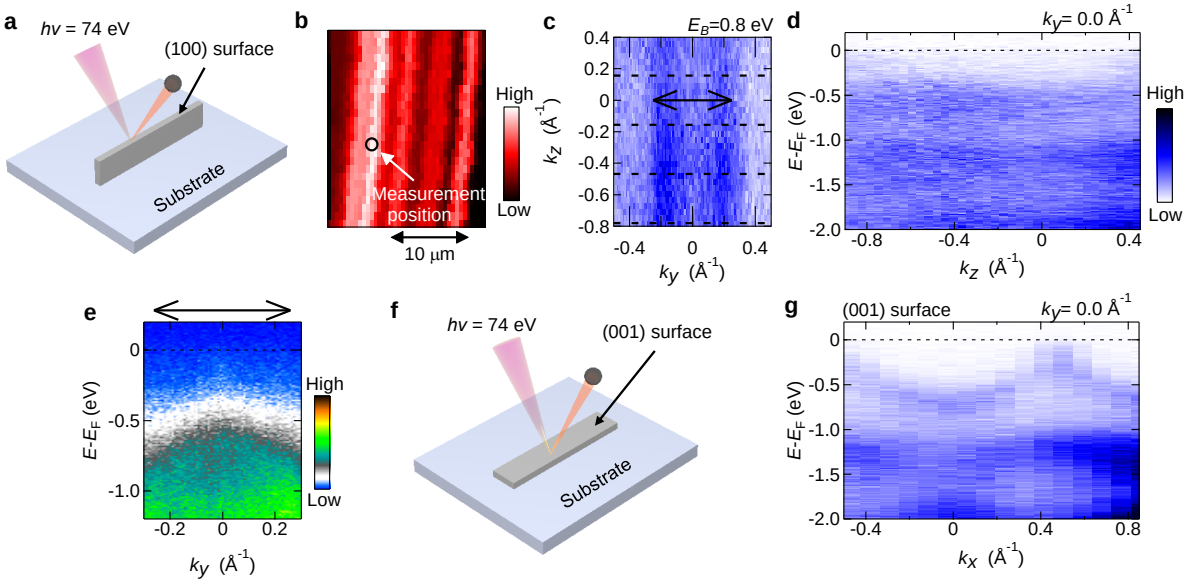

FIG. S9. **a,** Schematic of nano-ARPES of the side-surface (100). **b,** Photoelectron intensity distribution on the side surface of Bi_4Br_4 in the real space. The ARPES results shown in **c-e** were taken at the brightest position indicated by the black circle in this image. **c,** ARPES map along a k_y-k_z sheet plotted at $E - E_F = -0.8$ eV; here, k_y and k_z correspond to the directions parallel and perpendicular to the 1D chain, respectively. The measured intensity distribution is 1D-like, indicating that the photoelectrons are emitted from the (100) surface. Black dashed lines denote the periodicity of the surface Brillouin zone of the (100) surface. **d,** ARPES band map at $k_y = 0$ measured along k_z, which is perpendicular to the chain direction. **e,** ARPES band map along the black arrow in **c**, which is the chain direction (or k_y direction). **f,** Schematic of nano-ARPES for the top-surface (001). **g,** ARPES band map for the (001) surface at $k_y = 0$ measured along k_x, which is perpendicular to the chain direction. A clear periodicity corresponding to the (001) surface Brillouin zone is resolved. All of these images were taken with a sub-μm focused photon beam at $h\nu$=74 eV.

obtained from the top-surface (001) at the same condition, which exhibit a clear energy dispersion (Fig. S9g). These results are compatible with the crystal structure of Bi_4Br_4, which is quasi-1D and has the weakest bonding along the c-axis.

SUPPLEMENTARY NOTE 10: ESTIMATION FOR THE MAGNITUDE OF A BULK BAND GAP [FIG. S10]

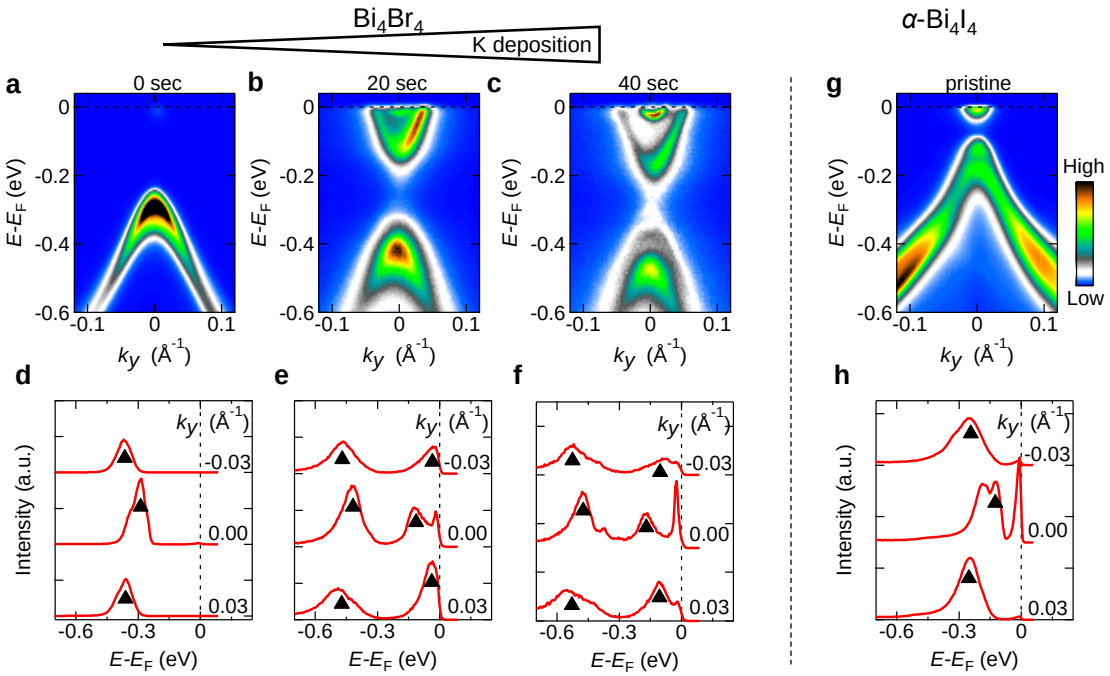

FIG. S10. **a-c,** ARPES intensity maps around the $\bar{M}$ point for different K coverages. **d-f** Energy distribution curves around the $\bar{M}$ point extracted from **a-c**. The black markers denote the position of the bulk band closest to the bulk band gap. **g,** ARPES intensity map around the $\bar{M}$ point for pristine α-Bi_4I_4. **h,** Energy distribution curves around the $\bar{M}$ point extracted from **g**.

The deposition of alkali atoms on the sample surface dopes negative charges, and thus it has been commonly used to investigate the band structure above the Fermi level. This technique has also been adopted in our study with a laser-based ARPES to estimate the magnitude of a bulk band gap in Bi_4Br_4. We have performed a series of measurements changing the time of deposition to increase step by step the coverage of potassium (K) atoms on the sample surface. Figures S10a-c display the ARPES dispersion around $\bar{M}$ obtained before and after K-deposition for 20 and 40 seconds, respectively; the conduction band is clearly visible below the Fermi level after the deposition. The magnitude of the

bulk band gap is estimated to be around 0.3 eV by comparing the peak positions of the bulk conduction band and the bulk valence band in EDC at the $\bar{\mathrm{M}}$ point, as most evident in Fig. S10e. This gap magnitude is more than two times larger than that of α-Bi_4I_4, which is estimated to be around 0.1 eV (Figs. S10g and S10h).

SUPPLEMENTARY NOTE 11: COMPARISON OF PHOTOEMISSION INTENSITIES OF THE TOPOLOGICAL DIRAC STATES IN BI_4X_4 (X=BR, I) [FIG. S11]

Here, we verify that Bi_4Br_4 is a HOTI through the comparison of photoemission intensities of in-gap states among three compounds: α-Bi_4I_4 (trivial insulator), β-Bi_4I_4 (WTI), as well as Bi_4Br_4. Fig. S11a compares ARPES intensity maps of these measured at the same

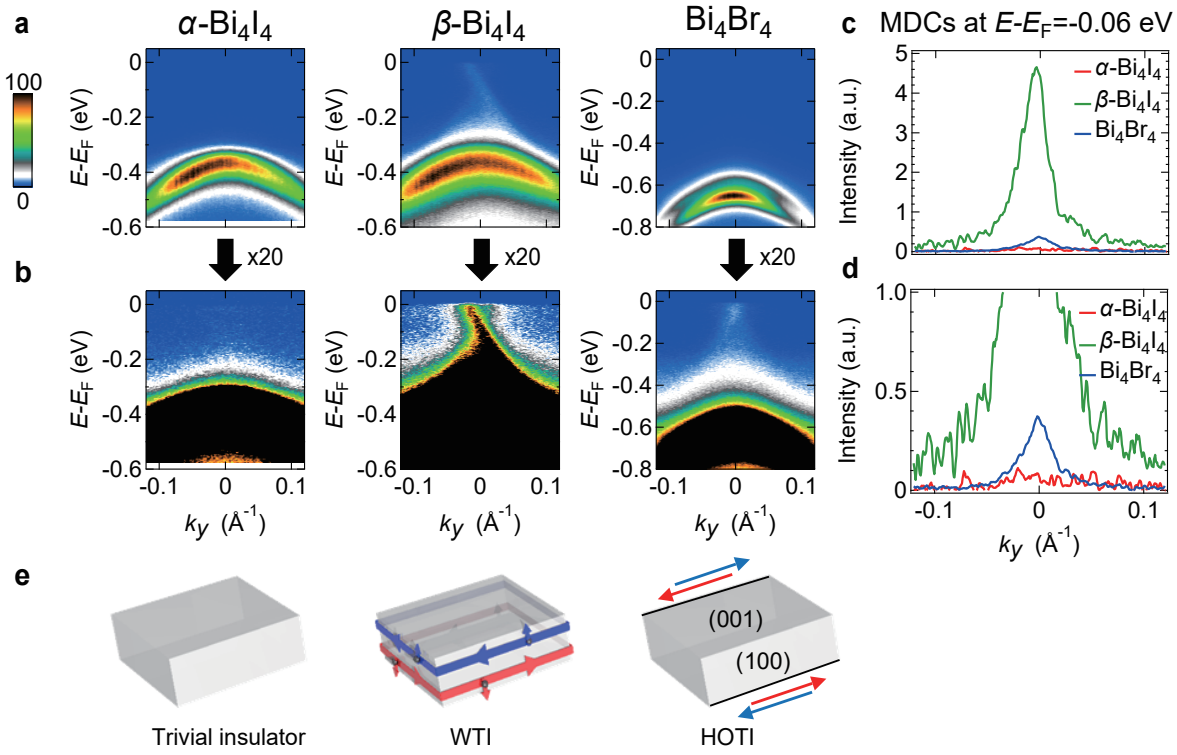

FIG. S11. **a,** ARPES intensity plots for α-Bi_4I_4, β-Bi_4I_4 and Bi_4Br_4 taken along the normal emission with respect to the *ab* cleavage plane. **b,** Same as **a**, but the color contrast in the image is changed by a factor of 20 to enhance the visibility of the topological in-gap states. **c,** Momentum distribution curves (MDCs) at $E - E_{\mathrm{F}} = -0.06$ eV, which is about the energy for the Dirac point in Bi_4Br_4. **c,** The same data as in **d**, but zoomed in the vertical axis. **e,** Schematics of topological properties of Bi_4I_4 and Bi_4Br_4. The ARPES data for Bi_4I_4 are reproduced from [4].

experimental setup. In these panels, the spectral intensities are normalized to those of the bulk band in each compound. The difference among the three is clear: while the in-gap Dirac dispersion is clearly visible in β-Bi_4I_4, it is not in the other two compounds (α-Bi_4I_4 and Bi_4Br_4). The Dirac state, however, shows up in the data of Bi_4Br_4 when the color contrast in the image is changed by a factor of 20 (Fig. S11b). Contrasting to it, the in-gap state never appears in the image for α-Bi_4I_4, no matter how much the color contrast is changed.

These intensity differences are further demonstrated in Fig. S11c and that zoomed in intensity (Fig. S11d), which plot momentum distribution curves (MDCs) at the energy of $E - E_F = -0.06$ eV. No peak relevant with the Dirac state is detected in α-Bi_4I_4, which is thus regarded as a trivial insulator. In contrast, the data of β-Bi_4I_4 and Bi_4Br_4 both exhibit a peak for the Dirac state; most importantly, the peak intensity is found to be much smaller in Bi_4Br_4 than in β-Bi_4Br_4, and this interrelation between the two compounds has been reproduced in several pieces of crystals from different batches. This result is, therefore, consistent with the theoretical prediction that the in-gap Dirac state of Bi_4Br_4 is confined within limited regions along the crystal hinges (Fig. S11e), which differs from the in-gap Dirac state of β-Bi_4I_4 extending over the side surface; the ARPES intensities should be smaller in Bi_4Br_4, as observed by ARPES measurements.

SUPPLEMENTARY NOTE 12: CONSISTENCY IN THE ARPES INTENSITIES OF THE DIRAC STATE OF BI_4BR_4 [FIG. S12]

In Supplementary Note 11, we demonstrate that the intensity of the in-gap Dirac state in Bi_4Br_4 is much weaker than that in β-Bi_4I_4 (a weak TI); this supports our conclusion that Bi_4Br_4 is a higher-order TI with topological hinge states much less in density than the topological edge states of a weak TI, which spread over surfaces. The reliability of such intensity comparison is guaranteed by our experiments of X-ray scattering (or GISAXS), which revealed that the condition of cleavage surfaces are similar between these two compounds. We note here that the image of X-ray scattering was taken from the same cleavage surface as that measured by ARPES in both cases of Bi_4Br_4 and β-Bi_4I_4; more specifically, we measured the cleaved surface by ARPES first, then brought the same sample piece mounted on the ARPES holder to a synchrotron facility to take X-ray scattering images from these surfaces.

While the careful experiments as mentioned above justify our conclusion, it would still be worth considering the condition of cleavage surfaces of Bi_4Br_4 and β-Bi_4I_4 to avoid any concerns on our results. Importantly, these compounds are built from chains bonded together by van der Waals forces, so that the top (001) and side (100) planes are both naturally cleavable. It is, thus, unlikely that one of these planes is dominantly exposed on a cleavage surface. In most cases, a huge number of small domains both for (001) and (100) planes should be left on the surface after cleaving; it is highly possible that the numbers of these domains and the ratio between the two become similar for different cleavage surfaces, according to a consideration of statistical mechanics. Furthermore, a laser of $\sim$50 μm in a spot size we used in ARPES covers enough area of the cleavage surface, allowing a fair comparison of spectral intensities for topological states between Bi_4Br_4 and β-Bi_4I_4.

To experimentally confirm this, we have repeated ARPES measurements on different cleavage surfaces from several crystal pieces of Bi_4Br_4. Very importantly, we have reproduced similar intensities of in-gap Dirac state, which are much weaker than that of β-Bi_4I_4; this

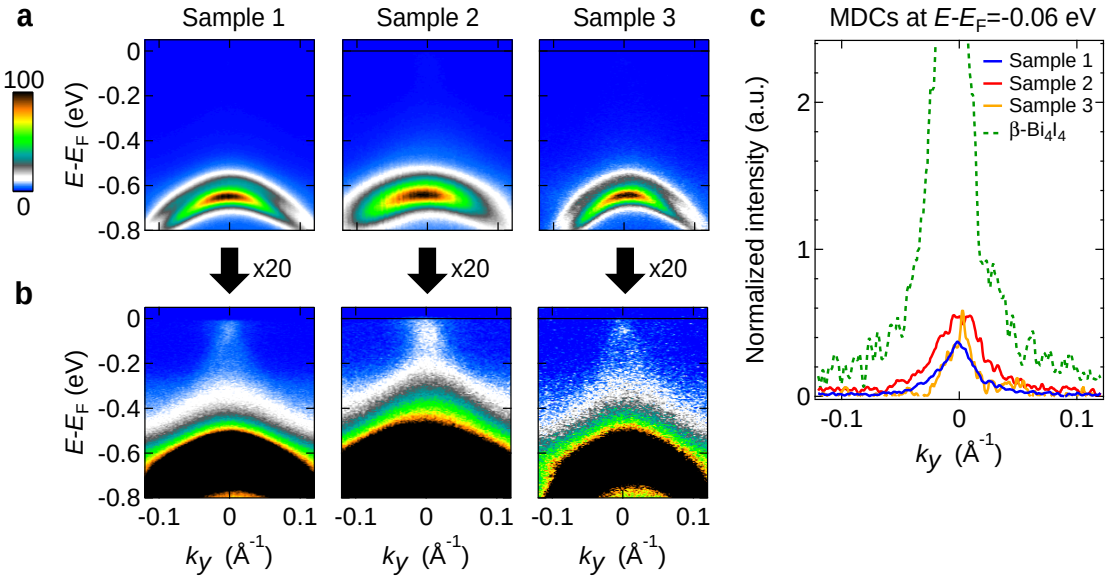

FIG. S12. **a,** ARPES intensity plots taken for different cleavage surfaces from several crystal pieces of Bi_4Br_4. The image for sample 1 is the duplicate of the main Fig. 4d. **b,** Same as **a**, but the color contrast in the images is changed by a factor of 20 to enhance the visibility of the topological hinge states. **c,** Momentum distribution curves (MDCs) at $E - E_F = -0.06$ eV, which is about the energy for the Dirac point in Bi_4Br_4. The MDC curve for β-Bi_4I_4 is also plotted with a dashed line to compare the ARPES intensities for the Dirac states between the two compounds.

result experimentally justifies our argument on the intensity comparison. A relevant data set of ARPES is plotted in Fig. S12. For a fair comparison, the ARPES spectra are normalized with respect to those of the bulk bands. While the Dirac dispersions are hardly visible in the images of Fig. S12a with the same color scale as in the main Fig. 4d, the in-gap states get clearly revealed when the color contrast is changed by a factor of 20 (Fig. S12b). From different sample pieces, the intensities of the Dirac states at E-$E_{\rm F}$ = -0.06 eV are repeatedly estimated to be within the range of 0.3-0.6% of those in the bulk states (Fig. S12c), which are much smaller than that of the Dirac state observed in β-Bi_4I_4 ($\sim$5%). The difference of the photoemission intensities by $\sim$10 times between these two compounds is ascribed to reflect the different densities of the topological states between a higher-order topological insulator (Bi_4Br_4) and a weak topological insulator (β-Bi_4I_4).

SUPPLEMENTARY NOTE 13: SPIN-RESOLVED ARPES OF BI_4BR_4 [FIG. S13]

We have also utilized a spin-ARPES technique to distinguish between topological surface state and topological hinge state; the laser beam in this experiment has the spot size of $\sim$ 50 μm, thus it illuminates a sufficient area of the cleavage surface, covering the top (010) plane, the side (100) plane and hinges that lie between these two planes. In this set-up, a spin-polarized signature should be obtained in a WTI, which forms band dispersions with spin-polarization on the side surface, as depicted in the Fig. S13a. In contrast, the spin polarization should not be detected in a HOTI because of the following reason: the ARPES signals are accumulated from two types of hinge states (Hinge-A and Hinge-B as shown in Fig. S13b), which are oppositely spin-polarized in the same momentum direction due to the C_2 symmetry of the crystal structure. Hence, the ARPES intensities for up- and down-spin are integrated to cancel the spin-polarization in the spectra

The experimental data are plotted in Figs. S13c and S13d for β-Bi_4I_4 and Bi_4Br_4, respectively. In β-Bi_4I_4 (Fig. S13c), the spin-polarization was confirmed to be inversed between $+k$ and $-k$, as expected in the observation of the topological side-surface [4]. In contrast, the sign inversion of spin-polarization was not observed in Bi_4Br_4; up-spin signals detected both at $+k$ and $-k$ most likely comes from the matrix element effect in photoemission, which occasionally yields an offset in spin-polarization ($\Delta I/I$) [8–10]. The clear difference between the spin-ARPES data between the two compounds strongly supports our conclusion

that the 1D Dirac state detected in Bi_4Br_4 originates from hinge states.

Here we add a couple of remarks: In general, the spin polarization detected by spin-resolved ARPES (SARPES) is the summation between intrinsic spin signals due to the initial state of electrons in solids and offset spin signals due to the final states in photoemission called as matrix element effect, which comes from not-perfect experimental geometry. To understand our data, two facts should be kept in mind: (1) The magnitude of the offset spin signal (ΔI) is proportional to the spectral intensity (I). (2) The spectra of Dirac states near E_F are hardly affected by the background intensities derived from bulk states, which are

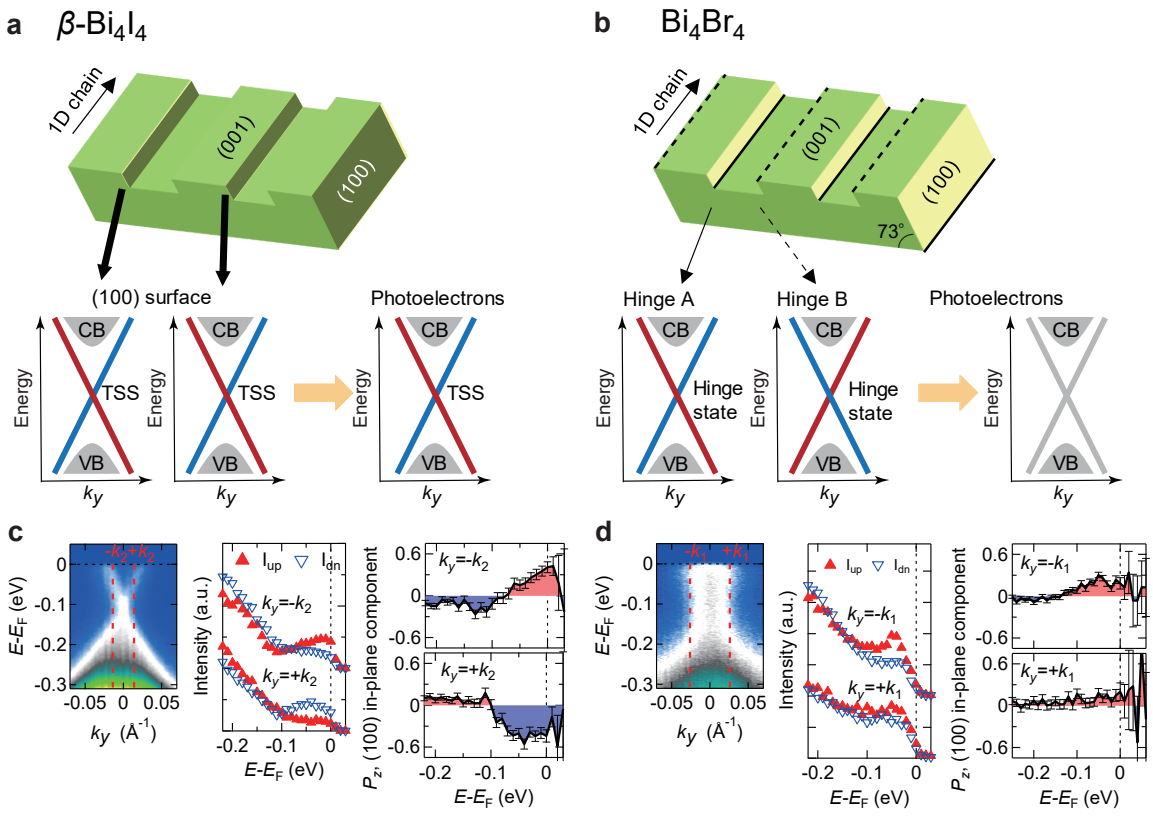

FIG. S13. **a, b,** Schematics of spin-polarized topological edge-state and the expected spectra of spin-resolved ARPES for Bi_4Br_4 (**a**) and β-Bi_4I_4 (**b**). **c, d,** Spin-resolved ARPES spectra for the z component [that is, the (100) in-plane component] of Bi_4Br_4 (**c**) and β-Bi_4I_4 (**d**). The measured k_y points are indicated by the red dashed lines in corresponding ARPES images (the left panels). Up-spin intensities (I_{up}) and down-spin intensities (I_{down}) are shown with red and blue markers (the middle panels), and the corresponding spin-polarizations are shown by red and blue areas (the right panels), respectively. The ARPES result of Bi_4Br_4 (left panel in **d**) is duplicated from the main Fig. 4f (cut 5). The data for β-Bi_4I_4 are reproduced from [2].

far from E_F in energy; even in Bi_4Br_4, Dirac states are dominant in the spectral intensity. These two facts mean that neither the offset spin signals nor the background from bulk states ruins our argument, allowing the fair comparison between the spin polarizations of Bi_4Br_4 (a higher-order TI) and β-Bi_4I_4 (a weak TI), which have different densities of topological edge states.

SUPPLEMENTARY NOTE 14: TEMPERATURE DEPENDENCE OF ELECTRICAL RESISTIVITY OF QUASI-1D BISMUTH HALIDES BI_4X_4 (X=BR, I) [FIG. S14]

We have argued above (Supplementary Notes 11, 12 and 13) that comparison of ARPES data among series materials reasonably leads to our conclusion. Here, we further note that transport behaviors (temperature evolution of resistivity) which exhibit clear differences among them are also consistently understood by accepting that α-Bi_4I_4, β-Bi_4I_4, and Bi_4Br_4 are a trivial insulator, a WTI, and a HOTI, respectively. Our conclusion, therefore, is not relying only on the ARPES results, but it is rather robust.

Since the resistivity of a topological insulator is affected by both semiconducting bulk states and topological edge states, its behavior with temperature, $\rho(T)$, is not straightforward [11]. Especially note that the combinational behavior of bulk and hinge states has not been discussed before in any literatures because there had not existed a HOTI in real materials so far; Bi_4Br_4 provides the first chance for such a study.

In a typical insulator, $\rho(T)$ exponentially increases (or accelerates in magnitude) with decreasing temperature. In stark contrast, our data of Bi_4Br_4 show a deaccelerating behavior toward the lowest temperature, as shown in Fig. S14. As a result, the variation of resistivity from 300 K to 2 K is only a factor of four, which is not possible in ordinary insulators and semiconductors. The most probable interpretation is that the $\rho(T)$ around the room temperature is dominated by thermally excited carriers in the insulating states of bulk, whereas that at low temperature below 50 K is dominated by the metallic hinge states. Such competition may also yield a plateau-like feature in the middle temperature range of 100 K and 200 K.

The characteristic behavior of $\rho(T)$ in Bi_4Br_4 would get more understandable by a comparison with those in sister materials, α- and β-Bi_4I_4, which are a trivial insulator and a

WTI, respectively [4]. Importantly, previous ARPES results have revealed that the bulk gaps of α- and β-Bi_4I_4 are ~0.1 eV, which is three times smaller than that of Bi_4Br_4 (~0.3 eV; see Fig. S10). Therefore, if we could ignore the contribution of topological edge states to $\rho(T)$, one can expect that the magnitude of $\rho(T)$ is always much larger in Bi_4Br_4 than in

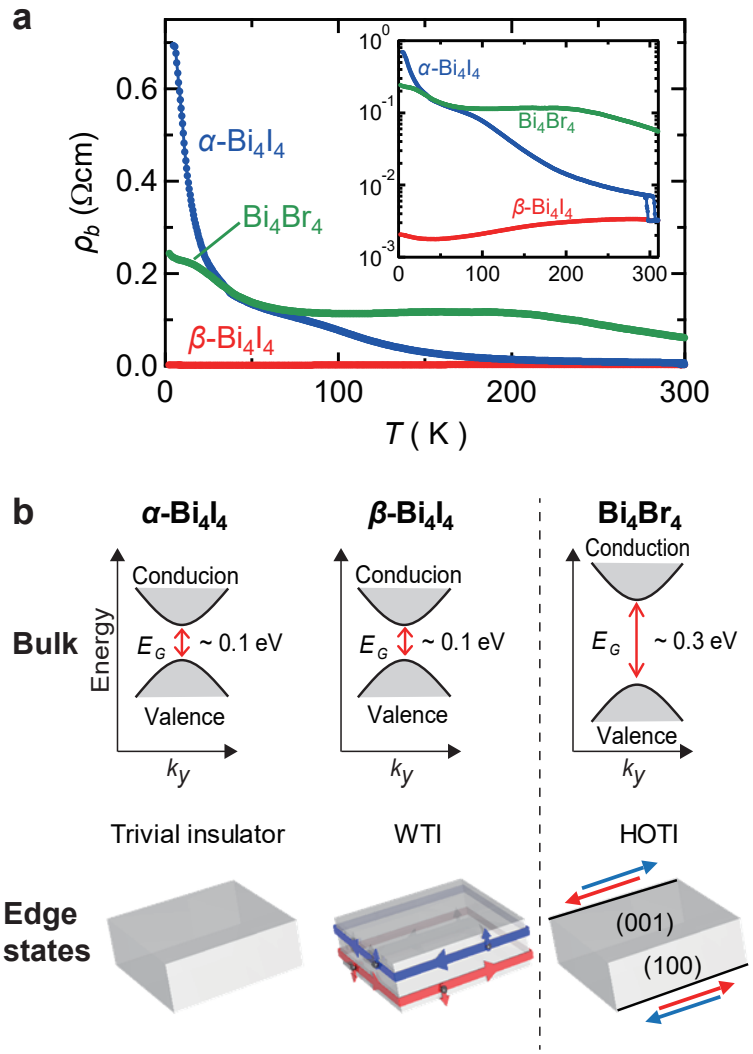

FIG. S14. **a,** Temperature dependence of the electrical resistivity in α- and β-Bi_4I_4 as well as Bi_4Br_4. The data for α- and β-Bi_4I_4 are reproduced from [4]. **b,** Schematics of the bulk band and topological edge-state of the three compounds. The band gap of Bi_4Br_4 ($\sim$ 0.3 eV) is three times larger than that of Bi_4I_4 ($\sim$ 0.1 eV). While this is compatible with the resistivity of Bi_4Br_4 which becomes largest among the three at high temperatures, the magnitude becomes smaller than that of α-Bi_4I_4 (trivial insulator) across $\sim$ 50 K with decreasing temperature; this behavior is most likely because metallic hinge states of Bi_4Br_4 (HOTI) get dominant as conducting carriers at low temperatures.

Bi_4I_4 regardless of temperature. This expectation is fulfilled between β-Bi_4I_4 (a WTI) and Bi_4Br_4. It is, in contrast, failed between α-Bi_4I_4 (a trivial insulator) and Bi_4Br_4: while $\rho(T)$ is much larger ($\sim$10 times larger) in Bi_4Br_4 than α-Bi_4I_4 at high temperatures, this relationship is reversed below 50 K. Importantly, however, these results are reasonably understood by accepting that metallic hinge states exist in Bi_4Br_4; although the hinge states have an only small amount of metallic carriers, these can dominate $\rho(T)$ at low temperatures, where thermal excitation of carriers in the insulating bulk should be negligible.

---

[1] Ozaki, T. Variationally optimized atomic orbitals for large-scale electronic structures. *Phys. Rev. B* **67**, 155108 (2003).

[2] Perdew, J. P., Burke, K. & Ernzerhof, M. Generalized gradient approximation made simple. *Phys. Rev. Lett.* **77**, 3865-3868 (1996).

[3] Liu, C.-C., Zhou, J.-J., Yao, Y. & Zhang, F. Weak Topological Insulators and Composite Weyl Semimetals:
β-Bi_4X_4 (X=Br, I). *Phys. Rev. Lett.* **116**, 066801 (2016).

[4] Noguchi, R. *et al.* A weak topological insulator state in quasi-one-dimensional bismuth iodide. *Nature* **566**, 518–522 (2019).

[5] Lai, K., Kundhikanjana, W., Kelly, M. & Shen, Z. X. Modeling and characterization of a cantilever-based near-field scanning microwave impedance microscope. *Rev. Sci. Instrum.* **79**, 063703 (2008).

[6] Hsu, C.-H. *et al.* Purely rotational symmetry-protected topological crystalline insulator α -Bi_4Br_4. *2D Mater.* **6**, 031004 (2019). URL `https://iopscience.iop.org/article/10.1088/2053-1583/ab1607`.

[7] Dudin, P. *et al.* Angle-resolved photoemission spectroscopy and imaging with a submicrometre probe at the SPECTROMICROSCOPY-3.2L beamline of Elettra. *J. Synchrotron Radiat.* **17**, 445-450 (2010).

[8] Heinzmann, U. and Dil, J. H. Spin-orbit-induced photoelectron spin polarization in angle-resolved photoemission from both atomic and condensed matter targets. *J. Phys. Condens. Matter* **24**, 173001 (2012).

[9] Jozwiak, C. *et al.* Widespread spin polarization effects in photoemission from topological

insulators. Phys. Rev. B **84**, 165113 (2011).

[10] Okuda, T. *et al.* Experimental Evidence of Hidden Topological Surface States in $PbBi_4Te_7$. *Phys. Rev. Lett.* **111**, 206803 (2013).

[11] Ren, Z., Taskin, A. A., Sasaki, S., Segawa, K. & Ando, Y. Optimizing $Bi_{2-x}Sb_xTe_{3-y}Se_y$ solid solutions to approach the intrinsic topological insulator regime. *Phys. Rev. B* **84**, 165311 (2011).